

A directed continuous-wave search from Scorpius X-1 with the five-vector resampling technique

Francesco Amicucci^{1,2}, Paola Leaci^{1,2}, Pia Astone¹, Sabrina D’Antonio³, Stefano Dal Pra⁴, Matteo Di Giovanni^{1,2}, Luca D’Onofrio¹, Federico Muciaccia^{1,2}, Cristiano Palomba¹, Lorenzo Pierini¹, Akshat Singhal⁵

¹INFN, Sezione di Roma, I-00185 Roma, Italy

²Università di Roma “La Sapienza”, I-00185 Roma, Italy

³INFN, Sezione di Roma Tor Vergata, 00133 Roma, Italy

⁴INFN, CNAF, 40127 Bologna, Italy

⁵HBCSE, Tata Institute of Fundamental Research, Mumbai 400088, India

E-mail: francesco.amicucci@roma1.infn.it and paola.leaci@roma1.infn.it

March 2024

Abstract. Continuous gravitational-wave signals (CWs), which are typically emitted by rapidly rotating neutron stars with non-axisymmetric deformations, represent particularly intriguing targets for the Advanced LIGO-Virgo-KAGRA detectors. These detectors operate within sensitivity bands that encompass more than half of the known pulsars in our galaxy existing in binary systems (i.e., over 417 pulsars), which are the targeted sources of this paper. However, the detection of these faint signals is especially challenged by the Doppler modulation due to the source’s orbital motion, typically described by five Keplerian parameters, which must be determined with high precision to effectively detect the signal. This modulation spreads the signal across multiple frequency bins, resulting in a notable reduction of signal-to-noise ratio and potentially hindering signal detection. To overcome this issue, a robust five-vector resampling data-analysis algorithm has been developed to conduct thorough directed/narrowband CW searches at an affordable computational cost. We employ this methodology for the first time to search for CWs from Scorpius X-1, using publicly available data from the third observing run of the Advanced LIGO-Virgo-KAGRA detectors. No statistically significant CW signals can be claimed. Hence, we proceeded setting 95% confidence-level upper limits in selected frequency bands and orbital parameter ranges, while also evaluating overall sensitivity.

1. Introduction

Gravitational waves (GWs) are a fundamental prediction of Albert Einstein’s General Theory of Relativity [1, 2] and are emerging as a revolutionary breakthrough in astrophysics. These ripples in the fabric of spacetime carry crucial information on the dynamics and interactions of massive celestial objects, providing a new lens through

which we can explore the universe. Since their first direct detection in 2015 [3] by the Laser Interferometer Gravitational-Wave Observatory (LIGO) [4] and the Virgo collaboration [5], GWs have revolutionized our understanding of the cosmos, offering unprecedented insights into the most energetic and cataclysmic events in the universe [6].

Understanding GWs not only advances our knowledge of astrophysics, but also presents opportunities to test and refine our understanding of the Theory of Gravity.

Unlike transient GWs emitted by the merger of compact objects, there are much fainter, persistent/continuous GWs (CWs), which are being continuously emitted by a source that has quasi-periodic rotational frequency. Due to their weakness, we need to integrate for long observing times to accumulate an adequate signal-to-noise-ratio (SNR) [7]. Promising sources of CWs include neutron stars (NSs), the remnants of massive stellar cores after a supernova explosion, that can emit a continuous stream of GWs due to their asymmetrical shapes, non-uniform rotation, or other structural irregularities [8]. The most commonly accepted model suggests *mountains* supported by elastic and/or magnetic stresses, where the NS rotational frequency f_{rot} is related to the GW frequency f_{GW} by $f_{\text{GW}} = 2f_{\text{rot}}$ [9]. Detecting CWs would allow us to get a set of information that electromagnetic observations alone cannot achieve, such as information on NS quadrupolar deformation (i.e., ellipticity), NS properties (i.e., the range of NS masses, radii, population models), and in general cold dense matter Equation Of State properties [7]. A review of the last twenty years of efforts to detect CWs can be found in [10].

In this paper, we focus on Scorpius X-1, which is the brightest Low-Mass X-ray binary (LMXB) composed of a NS in a binary orbit with a low-mass normal star (i.e., its companion). A characteristic property of these systems is the inflow of gas from the companion star to the NS, in a process known as accretion [11, 12]. The by-product of accretion is the generation of X-rays: the more accretion, the more X-rays are produced.

An interesting astrophysical model predicts that the GW strain h_0 from a LMXB at the torque-balance level is proportional to the square root of the x-ray flux F_x [13, 12, 11]. Since Scorpius X-1 is the brightest LMXB known so far, we consider it as one of the most interesting potential CW sources. Scorpius X-1 ephemerides (obtained through electromagnetic observations) are summarized in table 1.

Table 1. Observed Parameters of the LMXB Scorpius X-1.

Parameter		Value	Units	Ref
right ascension ^a	α	16h 19m 55.067s		[14]
declination	δ	$-15^\circ 38'25.02''$		[14]
frequency	f_0	(unknown)	Hz	
projected semi-major axis	a_p	[1.45, 3.25]	ls	[15]
time of ascending node	t_{asc}	1078153676 ± 33	GPS s	[16]
		06/03/2014 15:07:40	UTC	
orbital period ^b	P	68023.92 ± 0.02	s	[16]
		0.7873139 ± 0.0000007	d	
eccentricity	e	≤ 0.0132		[16]
argument of periapsis	ω	$[0, 2\pi]$ (unknown)	rad	

Notes. Uncertainties are 1σ unless otherwise stated.

^a The sky position is determined to the microarcsecond and therefore can be treated as known in the present search.

Several CW searches targeting Scorpius X-1 have been conducted so far, such as the Viterbi “hidden Markov Model” method [17, 18], and the cross-correlation CrossCorr search [19, 20], which was recently improved by using efficient lattice-based template banks [21] and resampling techniques for efficient frequency computations [22, 23]. More recently, the resampling has been also used to develop a new search pipeline called BINARYWEAVE that employs a semicoherent \mathcal{F} -statistic StackSlide approach [24]. In the current work, we perform a directed/narrowband[‡] search for CWs from Scorpius X-1, using the binary five-vector methodology [14] to analyse, for the first time with this method, data from the third observing LIGO-Virgo-KAGRA science run (O3)[§] [25, 26].

The paper is organized as follows. In section 2 we summarize the main features of CWs and how they will be observed at the detector site. In section 3 we describe the five-vector resampling method for NSs in binary systems. In section 4 we present the results for a narrowband CW search from Scorpius X-1 using the O3 data. In section 5 we show 95% confidence-level upper limits in selected frequency bands and orbital parameter ranges. Finally, we summarize the main outcomes in section 6.

2. Signal model

The expected GW signal $h(t)$ from a nonaxisymmetric NS, at the time of arrival at the detector $t = t_{\text{arr}}$, can be written using the polarization ellipse as the real part of [27]

$$h(t_{\text{arr}}) = H_0 (H_+ A_+(t_{\text{arr}}) + H_\times A_\times(t_{\text{arr}})) e^{i\Phi_{\text{det}}(t_{\text{arr}})}, \quad (1)$$

where Φ_{det} is the signal phase in the detector frame, H_0 is the wave amplitude, $A_{+,\times}(t)$ are the time-dependent sidereal detector response functions and are linked to the

[‡] The search is narrowband in the sense that it can account for nonzero uncertainties in the orbital Keplerian parameters [14]

[§] O3 started on April 1, 2019 15:00:00 UTC (GPS 1238166018) and ended on March 27, 2020 17:00:00 UTC (GPS 1269363618).

antenna patterns functions; $H_{+,\times}$ are the complex polarization functions, which are given by

$$H_+ = \frac{\cos(2\psi) - i\eta_p \sin(2\psi)}{\sqrt{1 + \eta_p^2}}, \quad (2)$$

$$H_\times = \frac{\sin(2\psi) + i\eta_p \cos(2\psi)}{\sqrt{1 + \eta_p^2}}, \quad (3)$$

where ψ is the polarization angle, defined as the orientation of the major axis of the polarization ellipse relative to the celestial parallel of the source, measured counterclockwise, and η_p corresponds to the CW degree of polarization and is defined as

$$\eta_p = -\frac{2 \cos \iota_{\text{rot}}}{1 + \cos^2(\iota_{\text{rot}})}, \quad (4)$$

with ι_{rot} being the inclination angle of the star's rotation axis with respect to the line of sight. The η_p parameter varies in the range $[-1, 1]$, where $\eta_p = 0$ for a linearly polarized wave and $\eta_p = \pm 1$ for a circularly polarized wave ($\eta_p = 1$ if the circular rotation is counter-clockwise).

The two complex amplitudes satisfy the condition $|H_+|^2 + |H_\times|^2 = 1$. The time dependent sidereal detector response functions $A_+(t), A_\times(t)$ depend on the relative position between the source and the detector, which changes due to the Earth sidereal motion. Hence, they encode the signal amplitude modulation. For a ground based *L-shaped* detector, the sidereal response can be precisely characterized by five components in the Fourier transform, with the Fourier coefficients determined by the source position, as well as the detector location and orientation on Earth [28]. As discussed in [27] (1) is equivalent to the standard expression given by (4) in [29]. As it can be noticed, in (1) we work with H_0 rather than the classic strain amplitude h_0 , which -for the ideal case of a steadily spinning triaxial ellipsoid star emitting GWs only at twice the rotation frequency- is given by (see, e.g., [30]):

$$h_0 = \frac{16\pi^2 G}{c^4 r P^2} I_{zz} \epsilon = \quad (5)$$

$$= 1.05 \times 10^{-27} \left[\frac{f_{\text{GW}}}{100 \text{ Hz}} \right]^2 \left[\frac{10 \text{ kpc}}{r} \right] \left[\frac{I_{zz}}{10^{38} \text{ kg m}^2} \right] \left[\frac{\epsilon}{10^{-6}} \right]. \quad (6)$$

We note that r is the distance to the source, I_{zz} is the source's moment of inertia along the star rotation axis \hat{z} , c is the speed of light, G is the universal gravitational constant and ϵ is the ellipticity, which is a measure of the NS deformation, defined as

$$\epsilon \equiv \frac{|I_{xx} - I_{yy}|}{I_{zz}}. \quad (7)$$

The relation between these two amplitudes is the following [27]

$$H_0 = \frac{h_0}{2} \sqrt{1 + 6 \cos^2 \iota_{\text{rot}} + \cos^4 \iota_{\text{rot}}}, \quad (8)$$

which is equal to $h_0/2$ for linear polarization and $h_0\sqrt{2}$ for circular polarization. We prefer using H_0 to avoid disentangling the information between h_0 and ι_{rot} . As shown

in (1), $h(t)$ is the product of two terms: the first, $(H_+A_+(t) + H_\times A_\times(t))$, is a ‘slow’ amplitude modulation, while the second, $e^{i\Phi(t)}$, is a ‘fast’ term, due to the intrinsic source frequency [27]. We use the method first presented in [27] to describe both signals and data in the Fourier domain at the five frequencies $f_{\text{GW}}, f_{\text{GW}} \pm f_{\text{sd}}, f_{\text{GW}} \pm 2f_{\text{sd}}$, where f_{sd} is the sidereal frequency^{||} (1.16×10^{-5} Hz).

3. The robust resampling technique

In principle, CWs can be detected by a single GW interferometer and are persistently present into any LIGO-Virgo-KAGRA dataset, allowing for detailed analysis. The way to search for CWs depends on the amount of information available about the source. The five-vector method is a frequentist pipeline [27, 31] based on the splitting at the detector of the expected GW frequency f_{GW} in five components due to the sidereal modulation of the Earth. This method is robust as it enables the detection of a signal with a given SNR, even in the presence of significant uncertainties in the orbital parameters [14].

As discussed in [14], a monochromatic GW signal undergoes multiple time-dependent modulations when it reaches the ground-based detector. Our goal is to compute the time series in a new time coordinate t' , using the *stroboscopic resampling*, i.e., the time series is downsampled at irregular intervals where the phase exhibits linear behavior. In other words, assuming that the original time series is evenly spaced, it is downsampled at the nearest integer values of the new time variable t' . It is important to note that, in the absence of spindown terms, stroboscopic resampling can be performed without prior knowledge of the frequency, as the time correction is independent of it.

The (monochromatic) signal phase in the (NS) source frame is

$$\Phi^{\text{NS}}(\tau) = \phi_0 + 2\pi f_{\text{GW}}(\tau - \tau_0), \quad (9)$$

where τ is the source emission time and ϕ_0 is the phase at the reference time τ_0 .

The signal phase observed at the detector frame is[¶]

$$\Phi^{\text{det}}(t_{\text{arr}}) = \phi_0 + 2\pi f_{\text{GW}} \left(t_{\text{arr}} + \frac{\mathbf{x}(t_{\text{arr}}) \cdot \hat{\mathbf{r}}}{c} - \frac{d}{c} - \frac{R(t_{\text{arr}})}{c} + \Delta_{\text{Ein},\odot} - \Delta_{\text{S},\odot} - \tau_0 \right), \quad (10)$$

where $\frac{\mathbf{x}(t_{\text{arr}}) \cdot \hat{\mathbf{r}}}{c}$ is the so-called Earth Rømer delay term, with $\mathbf{x}(t_{\text{arr}})$ being the vector from the *Solar System Barycentre* (SSB) to the detector, $\hat{\mathbf{r}}$ the unit vector from the SSB towards the *Binary System Barycentre* (BSB); d/c is the NS delay term with d the distance of the BSB to the SSB, $R(t)/c$ is the binary Rømer delay term [34, 35], with $R(t)$ being the radial distance of the CW-emitting NS from the BSB projected along the line of sight; while $\Delta_{\text{Ein},\odot}$ and $\Delta_{\text{S},\odot}$ are the Earth Einstein and Shapiro time delay, respectively [36, 37]. The term d/c is a constant term and can be neglected by

^{||} The Earth sidereal frequency is the inverse of sidereal period, which is ≈ 86164 s (≈ 23 h 56m 4s).

[¶] This expression, as reported e.g. in [10], is valid in the non-relativistic approximation $v/c \ll 1$, where v is the detector velocity with respect to the source. Since the heliocentric velocity of the detector is $|\mathbf{v}|/c \sim 10^{-4}$ and Scorpius X-1 linear heliocentric velocity is $|\mathbf{v}_{\text{NS}}|/c \sim 10^{-4}$ [32, 33], we can consider this approximation valid.

redefining the initial phase ϕ_0 . The binary delay $R(t)$ can be expressed in terms of five Keplerian parameters $\{P, a_p, e, \omega, t_p\}$, where a_p is the projected semi-major axis in ls, P is the time period required by a NS to complete its orbit around the BSB, e is the eccentricity, ω is the argument of periapsis, and t_p is the time of periapsis passage (see [34] and references therein). In the case of low eccentric orbit ($e \ll 1$), $R(t)$ can be equivalently parametrized by $\{\Omega, a_p, \kappa, \eta, t_{\text{asc}}\}$, where $\eta \equiv e \sin \omega$ and $\kappa \equiv e \cos \omega$ represent the *Laplace-Lagrange* parameters, t_{asc} is the time of ascending node and Ω is the mean orbital angular velocity. Hence, we can introduce the new time variable t' such that the phase $\Phi^{\text{det}}(t')$ is equal to the signal with constant frequency:

$$\Phi^{\text{det}}(t') = \phi_0 + 2\pi f_{\text{GW}}(t' - \tau_0), \quad (11)$$

with

$$t' = t_{\text{arr}} + \frac{\mathbf{x}(t_{\text{arr}}) \cdot \hat{\mathbf{r}}}{c} - \frac{d}{c} - \frac{R(t_{\text{arr}})}{c} + \Delta_{\text{Ein}, \odot} - \Delta_{\text{S}, \odot}. \quad (12)$$

It is evident that, by resampling the data according to (12), we can remove all modulations. In a hypothetical scenario, where both the detector and source are relatively stationary, i.e., all time correction terms are constant $t'(t_{\text{arr}}) = \text{const.}$, there will be no modulation, and therefore the signal will be monochromatic at the detector [14]. As previously mentioned, the key advantage of using a rescaled time for Doppler correction in narrowband searches is that t' does not depend on the frequency. This means that a single correction applies to all frequencies, making it especially useful for searching for a signal from Scorpius X-1, where the spin frequency is unknown. As explained in Section III of [36], for isolated sources, and in Appendix B of [14] for binaries NSs, we can take into account the spindown correction in a similar manner, although such correction is frequency-dependent. In this study, we assume no spindown, based on the expected steady-state torque balance scenario in LMXBs, which are our primary focus.

Once that we have properly demodulated the data to correct for both the Earth Doppler effect and binary orbital motion, the GW signal power is spread among five frequencies, related to the detector sidereal responses $A_{+, \times}$ in (1). For purely illustrative purposes, figure 1 shows the power spectrum of O3 Hanford data where a software-injected signal has been added with $H_0 = 1 \times 10^{-24}$ for $T_{\text{obs}} = 10$ days at a frequency 100.5 Hz, with sky location and orbital parameters of Scorpius X-1. Five-peaks are clearly visible, centered around the injection frequency, with a separation corresponding to the Earth sidereal frequency f_{sd} .

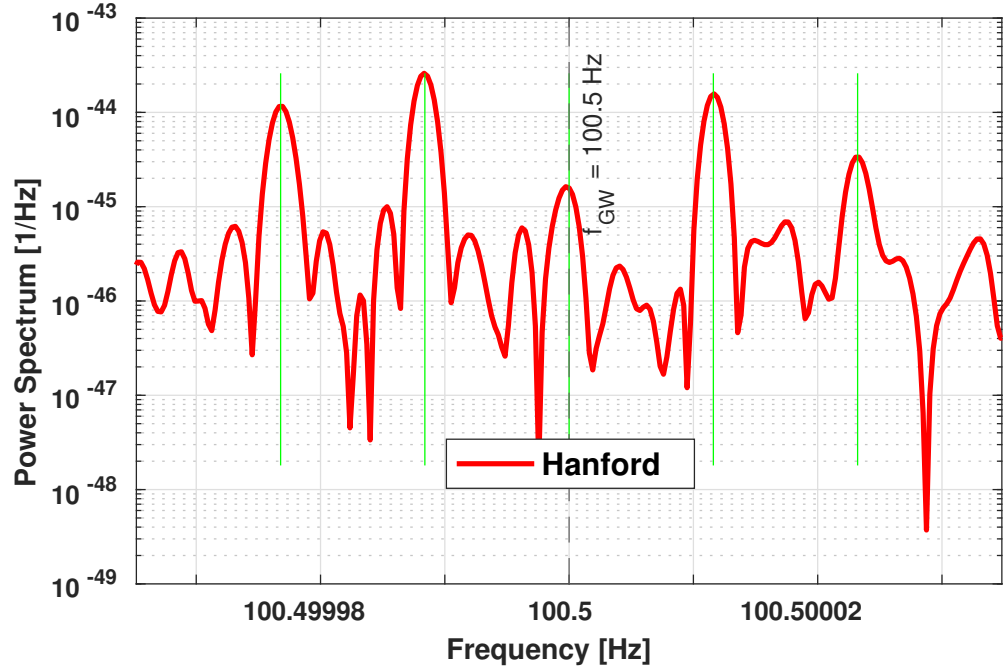


Figure 1. Power spectrum of a software injection Scorpius X-1 like signal at 100.5 Hz and with amplitude of 1×10^{-24} for $T_{\text{obs}} = 10$ days. We see five peaks in the frequency domain after the time-domain correction.

3.1. Matched filter and Detection statistic

CW search methods typically employ a matched-filtering approach, where a signal model is compared to the data to compute a Detection Statistic (DS) (e.g., see [38, 29]). Let us indicate the data time series

$$x(t) = h(t) + n(t),$$

where $h(t)$ and $n(t)$ are the GW signal and noise time series, respectively. If we apply the Doppler and relativistic corrections as described before, the signal is monochromatic apart from an amplitude and phase sidereal modulation. Equation (1) becomes

$$h(t) = H_0 (H_+ A_+(t) + H_\times A_\times(t)) e^{i(2\pi f_{\text{GW}} t + \phi_0)}, \quad (13)$$

where ϕ_0 is the phase at the time $t = 0$. Given a generic time series $g(t)$, we defined a five-vector as

$$\mathbf{G}(f) = \begin{pmatrix} G_{-2}(f) \\ G_{-1}(f) \\ G_0(f) \\ G_1(f) \\ G_2(f) \end{pmatrix}, \quad (14)$$

with

$$G_k(f) = \int_T g(t) \exp[-2\pi i(f - k f_{\text{sd}})t] dt, \quad \text{with } k = -2, \dots, 2 \quad (15)$$

where T is the observation time.

We therefore define the data five-vector \mathbf{X} and the signal template five-vectors $\mathbf{A}_{+, \times}$ for a frequency f as the Fourier components at the five frequencies where the signal power is split. We can also represent \mathbf{X} in terms of \mathbf{A}^+ and \mathbf{A}^\times , i.e., the source plus and cross five-vectors, respectively, which are the five Fourier-transform components of $A_{+, \times}(t)$. We then obtain [14]

$$\mathbf{X} = H_0 e^{i\phi_0} (H_+ \mathbf{A}^+ + H_\times \mathbf{A}^\times) + \mathbf{N},$$

where H_0 is given by (1) and \mathbf{N} is the five-vector of noise alone, which -in absence of a signal- would be [27]

$$\mathbf{N} = \int_T n(t) \exp[-2\pi i(f - k f_{\text{sd}})t] dt, \quad \text{with } k = -2, \dots, 2. \quad (16)$$

If the sky location is known, the source templates (\mathbf{A}^+ , \mathbf{A}^\times) can be used as a strong signature to match these five peaks, thereby allowing us to detect the signal. However, since the complex polarization functions (H_+ , H_\times) depend on the generally unknown ι_{rot} and ψ parameters, the exact source template cannot be computed. Hence, we compute the estimator for the polarization amplitudes individually by matched filtering source five-vectors (templates) with the data five-vectors [36]. An estimator for the polarization amplitudes, as a function of frequency, is defined as the scalar product between the data five-vector and the normalized source five-vector according to [39, 27]

$$\hat{h}^{+, \times}(f) = \frac{\mathbf{X}(f) \cdot \mathbf{A}^{+, \times}}{|\mathbf{A}^{+, \times}|^2}, \quad (17)$$

where $\hat{h}^{+, \times}(f)$ are estimators for the $+$, \times polarization amplitudes, respectively; the symbol ‘ \cdot ’ implies taking the complex conjugate of the second term. Based on the estimators computed in (17), we can construct a DS as a linear combination of the square of the norm of these estimators [27], as follows⁺:

$$\mathcal{S} = |\mathbf{A}^+|^4 |\hat{h}^+|^2 + |\mathbf{A}^\times|^4 |\hat{h}^\times|^2. \quad (18)$$

Since in a noiseless scenario the only non-zero Fourier components of a signal are at frequencies $\{f_{\text{GW}}, f_{\text{GW}} \pm f_{\text{sd}}, f_{\text{GW}} \pm 2f_{\text{sd}}\}$, the scalar product between the source templates and the data five-vectors will be non-zero at (up to) * nine different frequencies centred at f_{GW} [14], i.e. at $f_{\text{GW}} - m f_{\text{sd}}$ with $m \in [-4, 4]$. Hence, we observe that the five-peaks in figure 1 are transformed into a maximum of nine DS-peaks. This results from the cross-correlation between a five-peak template and a five-peak signal vector.

Assuming that the noise is Gaussian and white, with a mean of zero and a variance of σ^2 , from the definition of noise five-vector in (16), it follows that every component of the noise five-vector is also distributed according to a Gaussian with a mean of zero and a variance of $\sigma^2 \cdot T_{\text{obs}}$, with T_{obs} the total effective observation time. Hence, the probability density $f(\mathcal{S})$ in pure Gaussian noise is [36]

$$f(\mathcal{S}) = \frac{\exp(-\frac{\mathcal{S}}{\sigma^2 T_{\text{obs}} |\mathbf{A}^\times|^2}) - \exp(-\frac{\mathcal{S}}{\sigma^2 T_{\text{obs}} |\mathbf{A}^+|^2})}{\sigma^2 T_{\text{obs}} (|\mathbf{A}^\times|^2 - |\mathbf{A}^+|^2)}. \quad (19)$$

⁺ We clarify that the expression in [31] is not used. Instead, for simplicity, we adopt the formulation from [27], as this is not a multi-detector search.

* Depending on the SNR, a correctly demodulated signal may result into less than nine peaks.

For known sky location, $(\mathbf{A}^+, \mathbf{A}^\times)$ are source templates that are applied as a match-filter for detecting the signal. Consequently, the computation of the histogram of \mathcal{S} (such that the area under the curve is unity), follows the function in (19). By integrating (19), we obtain the probability to have a DS value above a given threshold \mathcal{S}^* , i.e.:

$$\begin{aligned} P(\mathcal{S} > \mathcal{S}^*) &= \int_{\mathcal{S}^*}^{\infty} f(\mathcal{S})d\mathcal{S} = \\ &= \frac{|\mathbf{A}^\times|^2 \exp(-\frac{\mathcal{S}^*}{\sigma^2 T_{\text{obs}} |\mathbf{A}^\times|^2}) - |\mathbf{A}^+|^2 \exp(-\frac{\mathcal{S}^*}{\sigma^2 T_{\text{obs}} |\mathbf{A}^+|^2})}{|\mathbf{A}^\times|^2 - |\mathbf{A}^+|^2}. \end{aligned} \quad (20)$$

3.2. Resampling pipeline

In figure 2 we have sketched the resampling pipeline flowchart. It commences from the creation of a Short Fast Fourier Transform (FFT) Database from detector calibrated data, the so-called SFDB [38, 40]. From this data, we extract a 1 Hz wide band, which is properly resampled in the time domain. Then, the DS is computed, and coincidences among detectors are performed to filter out false CW candidates (as outlined in section 3.4). If no candidate survives the coincidence veto, the resampling procedure can be repeated by adjusting the five Keplerian parameters of the target source used to define the new time variable in (12). This step is particularly important when the source ephemerides are not known with sufficient precision, as in the case of Scorpius X-1. In our approach, we varied these parameters by incorporating the maximum allowable offsets needed to detect CWs, as determined in a previous study [14]. Conversely, if a candidate survives the veto procedure, it necessitates a follow-up analysis to thoroughly assess the candidate and verify its significance. For example, a simple follow-up method involves studying the behavior of the SNR as a function of T_{obs} . In the case of a genuine CW signal, the SNR is expected to increase, at best in Gaussian noise, proportionally to the square root of T_{obs} [41]. A detailed explanation of the veto procedure, first described in [14], follows.

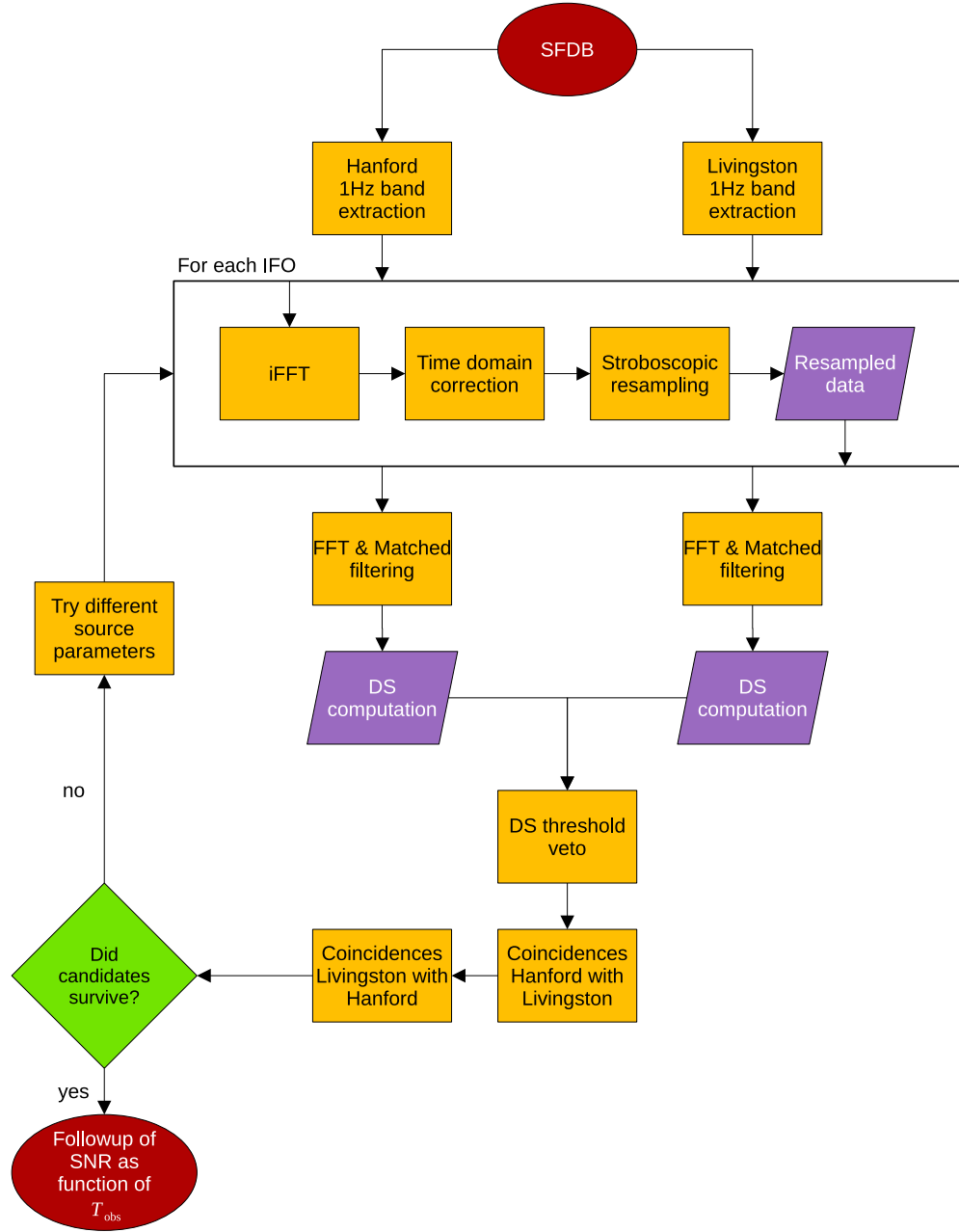


Figure 2. Workflow of the binary resampling algorithm to detect CWs from a binary NS.

3.3. DS veto procedure

For a given false alarm rate (FAR), we can use (20) to fix a threshold on the DS such that

$$P(\mathcal{S} > \mathcal{S}^*) \leq \frac{\text{FAR}}{\# \text{ of independent trials}} \equiv \text{NFAR}, \quad (21)$$

where the “# of independent trials” refers to the number of points in the search parameter space and is equal, in this specific case, to the number of frequency bins times the number of sets of binary search parameters. In this way we account for

the *look-elsewhere* effect [42] (a statistical phenomenon where an apparently significant observation may arise by chance due to the search parameter space size).

A candidate having a DS value higher than the threshold is less likely to be caused by Gaussian noise and needs to be deeply followed up. In the following, this will be called the DS veto. However, the presence of instrumental lines and data gaps cause deviations from this expected behavior. To mitigate their impact on data analysis, these lines are documented and often made publicly available, along with instructions on how to calculate their harmonics. The website [43] provides information on the known instrumental lines for the third observation run of the LIGO-Virgo-KAGRA collaboration. These deviations are more prominent towards the tail of the distribution when \mathcal{S} is large and are taken into account in the computation of the threshold, as detailed in [Appendix A](#). Rather than using \mathcal{S} , we follow [14] and compute \mathcal{S}' :

$$\mathcal{S}' = \frac{\mathcal{S} - \mu(\mathcal{S})}{\sigma(\mathcal{S})}, \quad (22)$$

which is a linear function of \mathcal{S} ; $\mu(\mathcal{S})$ and $\sigma(\mathcal{S})$ are the mean and standard deviation of \mathcal{S} across a given 1 Hz band, respectively. Finally, in the real O3 search, we set as a valid threshold a value of $\mathcal{S}'^* = 18$ (for further details see [Appendix A](#)).

3.4. Coincidence-based veto procedure

To discard candidates not caused by real CWs, we employ a coincident veto criterion described in [14]. Given a candidate at a frequency f_{cand} in a particular interferometer, the three coincidence veto consists of two main steps:

- (i) **Internal veto:** compute the coincidence with candidates found within the same detector. A candidate is discarded if there are fewer than $n_{\text{coin}}^{\text{int}}$ peaks above threshold in the same detector at the frequencies $f_{\text{cand}} + m f_{\text{sd}}$, $m \in [-4, 4]$; $n_{\text{coin}}^{\text{int}}$ is an integer varying between 1 and 9, but in the O3 search we have set it to three, as in the previous study [14].
- (ii) **Inter-detector veto:** compute the coincidences with candidates identified in the other detector. In the context of simultaneous observations of GW data by multiple detectors with the same T_{obs} and frequency resolution, it is expected that signal peaks will consistently align at the same (up to) nine DS-peak frequencies across all detectors. To distinguish true signals from instrumental noise, a candidate surviving the internal veto is rejected if fewer than n_{coin} peaks surpass the threshold at the frequencies $f_{\text{cand}} + m f_{\text{sd}}$, where $m \in [-4, 4]$, in the corresponding detector. Here, n_{coin} is an integer ranging from 1 to 9. Candidates failing to meet this criterion are likely to be artefacts. Also in this case, we have set it equal to three.

To be conservative, however, we use a certain tolerance that considers an extra frequency bin $\Delta f = 1/T_{\text{obs}}$ on either side of each of the expected nine DS-peaks frequencies, resulting, for a given candidate frequency f_{cand} , in a wider nine-peak coincidence interval

defined as

$$\bigcup_{m \in [-4, 4]} [f_{\text{cand}} + m f_{\text{sd}} - \Delta f, f_{\text{cand}} + m f_{\text{sd}} + \Delta f].$$

4. Results

The uncertainties in the electromagnetically measured binary period and time of ascending node for Scorpius X-1, as reported in table 1, exceed the maximum allowable offsets (in binary parameters) required to detect a genuine CW signal, as shown in [14] (see table 2). Hence, we used the Scorpius X-1 ephemerides from table 1 and offset parameters from table 2 to perform, for the first time, three real narrowband resampling searches for Scorpius X-1 like sources. These searches spanned the entire frequency range of [10 – 1000] Hz and the full O3 dataset. These 3 searches are enough to cover the full range between them, without additional templates being placed, since the method is robust enough to any combination of offsets within. Unlike [19], we did not exclude frequencies affected by narrowband instrumental disturbances [43] in our analysis, relying on our robust two-step veto procedure (section 3) to eliminate false candidates. This approach was validated using the two binary hardware injections [44] in the O3 dataset (Appendix B). As a result, we report all candidates, including those within the frequency ranges of O3 known instrumental lines [43].

Table 2. Set of parameter offsets we used for the binary demodulation step [14].

ΔP [ms]	Δa_p [mls]	Δe	$\Delta \omega$ [°]	Δt_p (s)
24	14	10^{-4}	0.01	0.1

The three real O3 searches we considered are characterized by null offset (i.e., assuming that the Scorpius X-1 ephemerides are really exact) $\{P, a_p, e, \omega, t_p\}$, a “+ offset” $\{P + \Delta P, a_p + \Delta a_p, e + \Delta e, \omega + \Delta \omega, t_p + \Delta t_p\}$ and a “– offset” $\{P - \Delta P, a_p - \Delta a_p, e - \Delta e, \omega - \Delta \omega, t_p - \Delta t_p\}$, respectively. The parameter space of the three sets is shown in table 3.

As previously mentioned, we neglect spindown terms. According to the results derived in section 3, we employ a threshold of $\mathcal{S}'^* = 18$ to select candidates in every 1 Hz frequency band. Out of approximately 3.06×10^{10} potential candidates, we identify a total of 184 726 candidates at Hanford and 52 527 at Livingston, respectively, when we correct for Doppler orbital modulation with a null offset. The distribution of these candidates among all 1 Hz frequency bands is shown in figure 3. After applying the three-coincidence veto to this set of surviving candidates, we find that no candidates remain. Similar values are obtained in the ‘+ offset’ and ‘– offset’ searches, which are detailed in table 4 for Hanford and in table 5 for Livingston, respectively..

Table 3. O3 narrowband search parameter space. We note that a_p might vary from 1.4 s and 3.25 ls, but we have arbitrarily chosen $a_p = 1.8$ ls and $\omega = 45.1^\circ$, as done in [14].

Parameter	Values			Units
	– offset	null offset	+ offset	
frequency	f_0 [10, 1000]	[10, 1000]	[10, 1000]	Hz
projected semi-major axis	a_p 1786	1800	1814	mls
time of periastris passage	t_p 1078161997.7	1078161997.8	1078161997.9	GPS s
orbital period	P 68023.896	68023.920	68023.944	s
eccentricity	e 0.0131	0.0132	0.0133	
argument of periastris	ω 45	45.1	45.2	degrees

Table 4. Number of candidates in the Hanford detector that survive various veto stages for every search. The \mathcal{S}^{*} value for the DS veto is 18.

Search	Initial candidates	DS veto	Coincidence veto	
			Internal	Inter-detector
– offset	$3.05692596 \times 10^{10}$	181 866	29 935	0
null offset	$3.05692596 \times 10^{10}$	184 726	9 979	0
+ offset	$3.05692596 \times 10^{10}$	182 946	9 756	0

Table 5. Number of candidates in the Livingston detector that survive various veto stages for every search. The \mathcal{S}^{*} value for the DS veto is 18.

Search	Initial candidates	DS veto	Coincidence veto	
			Internal	Inter-detector
– offset	$3.05692596 \times 10^{10}$	50 479	18 892	0
null offset	$3.05692596 \times 10^{10}$	52 527	21 620	0
+ offset	$3.05692596 \times 10^{10}$	51 257	20 753	0

It is important to note that, had any candidates survived the veto chain, we would have performed a thorough follow-up to investigate their origin. This would include using [45] in directed mode and passing the information to other pipelines [19, 17] for independent verification or further analysis.

5. Sensitivity estimation

We begin by setting upper limits in all 1 Hz frequency bands listed in the first rows of table 6, performing Monte-Carlo signal-injection studies using the same O3 search and veto-chain schemes. The goal is to find the h_0 value such that (at least) 95% of

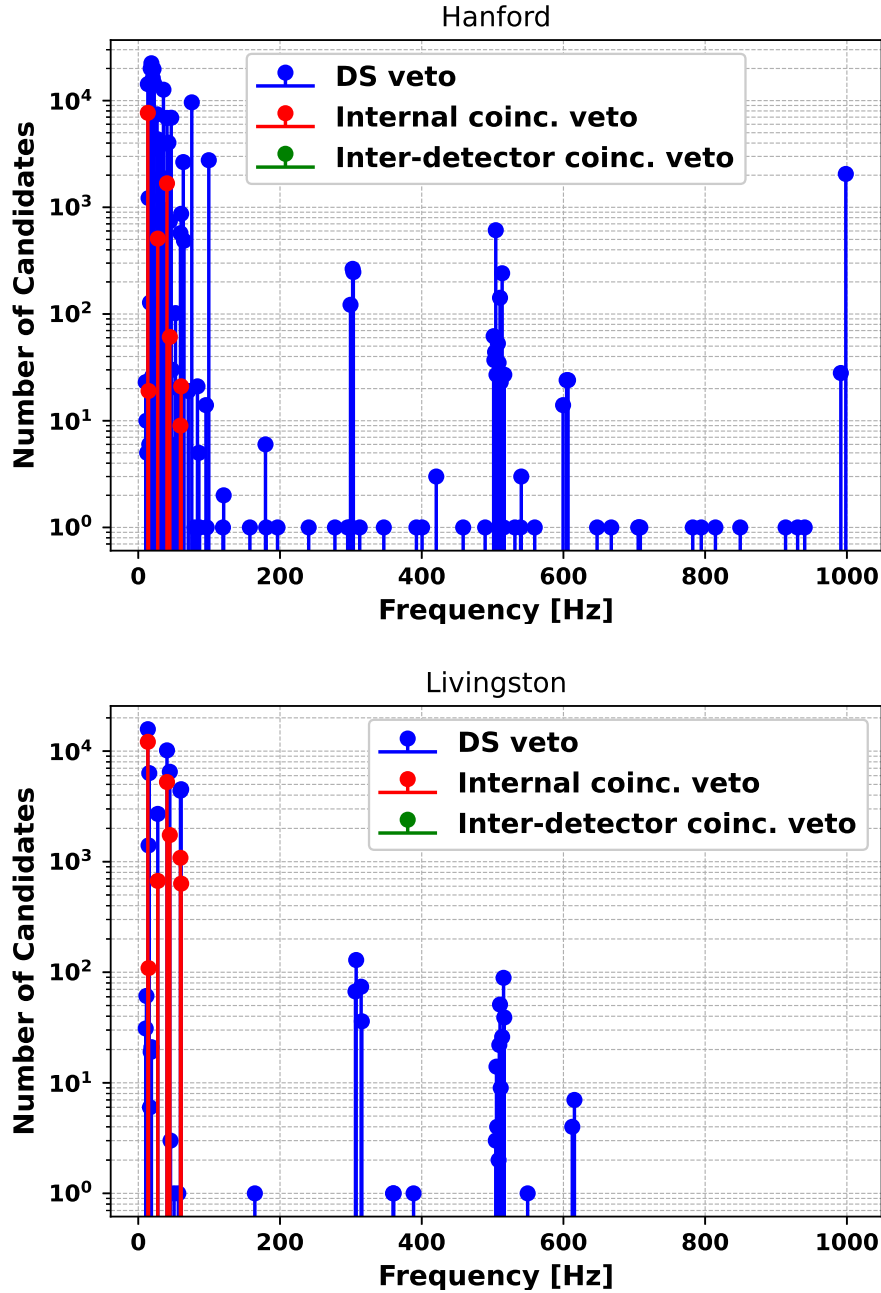


Figure 3. Number of candidates surviving the $\mathcal{S}'^* = 18$ veto for all 1 Hz wide frequency bands in the interval $[10, 1000]$ Hz for the real O3 "null offset" search for CWs from Scorpius X-1 in Hanford (*top*) and Livingston (*bottom*).

the signal injections would be recovered with this amplitude value and that are more significant than the most significant candidate identified in the real search in that band. In principle, this should be done by demodulating the injected signals using both the exact binary parameters from table 3 and the offset parameters from table 2. However, for simplicity and to reduce computational costs, we consider the first case and proceed as follows:

- In every 1 Hz frequency band in the first rows of table 6, starting from $H_0 = 1 \times 10^{-26}$ for the frequency ranges $\{[90, 91], [100, 101], [125, 126]\}$ Hz and $H_0 = 5 \times 10^{-26}$ for the other ones, we perform 4600 software injections in the whole O3 data, with source parameters $\{[P, P \pm \Delta P], [a_p, a_p \pm \Delta a_p], [e, e \pm \Delta e], [\omega, \omega \pm \Delta \omega], [t_p, t_p \pm \Delta t_p]\}$, where $\{P, a_p, e, \omega, t_p\}$ are the Scorpius X-1 ephemerides of table 3 and $\{\Delta P, \Delta a_p, \Delta e, \Delta \omega, \Delta t_p\}$ are uniformly drawn from the ranges shown in table 6. Frequency values were uniformly drawn from a subinterval of 0.3 Hz centered around the midpoint of each 1 Hz analyzed band ‡. We also extract ψ and $\cos \iota_{\text{rot}}$ from uniform distributions using the range shown in table 6.
- We compute the DS value for every injection data series and select the most significant candidate in the whole 1 Hz band ††.
- We consider an injected signal as *recovered* if we find a candidate with a value of \mathcal{S}' larger than the largest \mathcal{S}' value found in the real search, and in the same frequency band.
- The above condition must be met at least 95 times (out of 100) for a given amplitude H_0 to achieve a 95% confidence level. If this is the case, we can determine the corresponding upper limit. Otherwise, we repeat the procedure by increasing H_0 in steps of 2×10^{-26} .

Table 6. Source parameter ranges used to establish upper limits.

Parameter	Units	Range
Δf_0	Hz	[90,91], [100,101] [125,126], [222,223], [304, 305], [400,401], [500,501]
Δa_p	mls	[0,14]
Δt_p	GPS s	[0, 0.1]
ΔP	ms	[0, 24]
Δe		[0, 10^{-4}]
$\Delta \omega$	degree	[0,0.01]
ψ	rad	[0, 2π]
$\cos \iota_{\text{rot}}$		[-1,1]

To identify the corresponding value of H_0 for a given 1 Hz frequency range, we select the two closest values of injected H_0 , such that one has a recovery rate (p) below 95%, and the other is above. Let these points be (H_1, p_1) and (H_2, p_2) , where $p_1 < 0.95 \leq p_2$. We define the slope of the recovery curve as

$$b_{\text{slope}} = \frac{H_2 - H_1}{p_2 - p_1}. \quad (23)$$

‡ This approach is adopted to avoid border effects, which could complicate the detection of signals at the boundary between adjacent bands.

†† The coincidence veto is not considered in computing the upper limits, as no candidates survived the real search.

Using this slope, we perform a linear interpolation to estimate H_0 for $p = 0.95$, i.e:

$$H_0 = H_1 + b_{\text{slope}} \cdot (0.95 - p_1). \quad (24)$$

Finally, we compute the classical strain amplitude h_0 via

$$h_0 \approx 1.31 \cdot H_0. \quad (25)$$

The factor 1.31 comes from averaging (8) over a flat $\cos \iota_{\text{rot}}$ distribution.

Upper limits are computed using the CNAF HPC cluster [46]. To extend the analysis to other frequency bands, we apply the interpolation/extrapolation method used in [14]. However, given that our search spans the entire frequency range from 10 Hz to 1000 Hz, we instead utilized the maximum DS values found in every analyzed 1 Hz-wide band, rather than interpolating the upper limits using the interferometer noise sensitivity curve. The resulting sensitivity estimation versus frequency results are shown in figure 4, where it is also shown the theoretical strain (at the torque-balance level) assuming $M_{\text{NS}} = 1.4M_{\odot}$ and $R_{\text{NS}} \approx 10\text{km}$ [14]

$$h_0 \approx 3.5 \times 10^{-26} \sqrt{\frac{300\text{Hz}}{f_{\text{rot}}}}. \quad (26)$$

The ‘torque balance’ curve is included solely to facilitate comparison with existing literature.

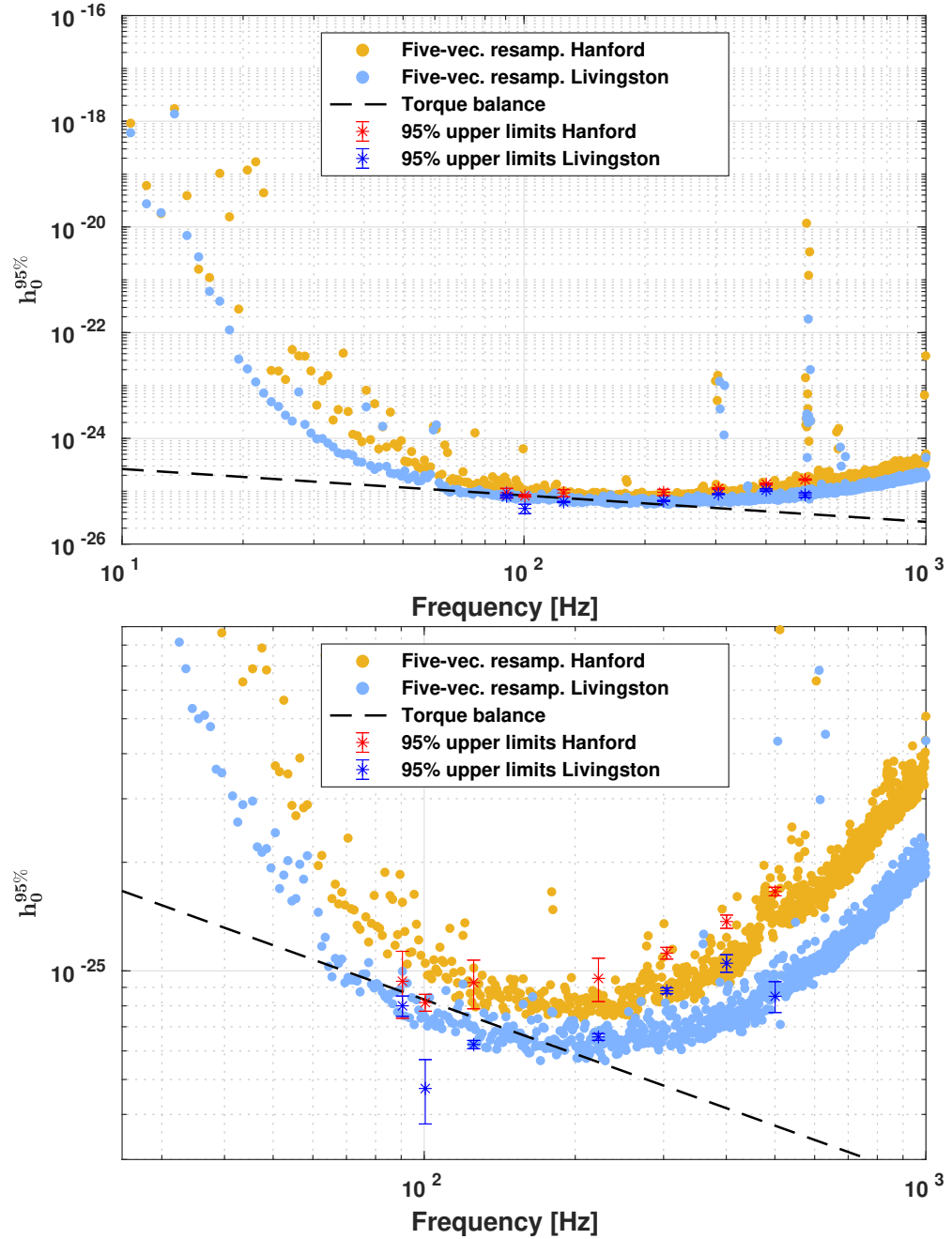


Figure 4. *Top:* Sensitivity estimation as a function of frequency for the Hanford (orange points) and Livingston (blue points) detectors. These estimates are extrapolated from the computed upper limits (marked with asterisks) with the maximum DS values found in every analyzed 1 Hz-wide band [47]. The Upper limits are computed in selected frequency bands and orbital parameter ranges. The vertical error bars indicate the statistical uncertainty on h_0 , computed as $\Delta h_0 = \sigma_{95\%} \cdot b_{\text{slope}}$, where σ_p is the binomial standard deviation for a recovery percentage of 95% using 100 injection: $\sigma_{95\%} = \sqrt{0.95(1 - 0.95)/100} \sim 0.022$. We note that the theoretical strain at the torque-balance level (light green dashed line) is obtained assuming $M_{\text{NS}} = 1.4M_{\odot}$ and $R_{\text{NS}} \approx 10$ km. *Bottom:* Zommed section of the above plot in the frequency range [25, 1000] Hz.

As discussed in [19], deriving firm conclusions about the NS equation of state or magnetic field strength from our upper limits is challenging without assuming a specific accretion model. We note that the most stringent sensitivity estimation value is at $f \approx 229.5$ Hz and is equal to $h_0 \approx 5.64 \times 10^{-26}$, which is 1.73 times better than the upper limit of the zero-eccentricity cross-correlation search at the same frequency [19] and 2.87 times better than the hidden Markov model Viterbi pipeline [17]. However, both the Cross-correlation and Viterbi searches explore the full prior range of orbital parameters, assuming circular orbits, whereas this search focused on a restricted region of the elliptical orbital parameter space.

To account for the different parameter spaces explored by these pipelines, we compute the sensitivity depth \mathcal{D} and the parameter-space breadth \mathcal{B} , as defined in Section 4 of [10]. The results obtained are $\mathcal{D} = 66.3$ at $f_{\mathcal{D}} = 206.8824$ Hz and $\lg \mathcal{B} = 12.1$. However, when using Equation (68) from [10] to compute the binary orbital parameter space, only three out of the five orbital parameters are considered in the metric, namely $\{a_p, P, t_{\text{asc}}\}$. Hence, we expect that the actual value of \mathcal{B} for the search presented in this paper would be higher if the remaining two parameters, $\{e, \omega\}$, were also included. In figure 5, we compare our results with those obtained from the Cross-correlation search in O3, the Viterbi search in O3, and the Resampling search in O2 [10].

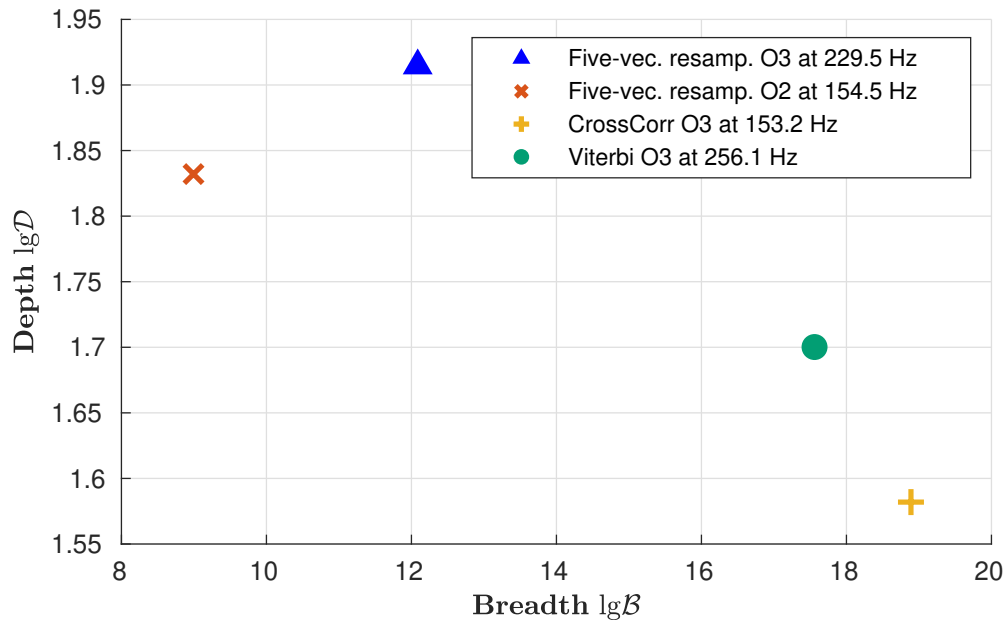


Figure 5. Sensitivity depth $\lg \mathcal{D}$ versus parameter-space breadth $\lg \mathcal{B}$ computed following [10]. The blue point represents the value obtained in this work, with the sensitivity depth \mathcal{D} taken from the most stringent value $h_0 \approx 5.54 \times 10^{-26}$ for the Livingston detector at $f_{\mathcal{D}} = 229.5$ Hz. Also displayed are the results for the model-based Cross-correlation search [19] and the hidden Markov model Viterbi search [17] on O3 data, and the five-vector Resampling search on O2 data [14], as reported in [10].

6. Conclusions

We applied the generalized five-vector resampling methodology to search for CWs from NSs in binary systems, focusing on the LMXB Scorpius-X1, across a range of GW signal frequencies $10 \text{ Hz} \leq f_0 \leq 1000 \text{ Hz}$, corresponding to NS spin frequencies of $5 \text{ Hz} \leq f_{\text{rot}} \leq 500 \text{ Hz}$. This is the first time such a technique is used to perform a real search in the O3 advanced LIGO–Virgo–KAGRA dataset. The uncertainties in the electromagnetically measured binary parameters of Scorpius X-1 are significantly larger than the maximum offsets in these parameters that we can use to detect a true CW signal without deliberately resorting to a matched-filtering approach, as indicated by a previous study [14]. Hence, we restrict our search to three orbital parameter configurations: one assuming the Scorpius X-1 ephemerides $\{P, a_p, e, \omega, t_p\}$ are exact, and two additional configurations where the parameters are adjusted by their respective maximum offsets, i.e., $\{P \pm \Delta P, a_p \pm \Delta a_p, e \pm \Delta e, \omega \pm \Delta \omega, t_p \pm \Delta t_p\}$, with $\{\Delta P = 24 \text{ ms}, \Delta a_p = 14 \text{ mls}, \Delta e = 10^{-4}, \Delta \omega = 0.01^\circ, \Delta t_p = 0.1 \text{ s}\}$ being the maximum values of binary-parameter offsets.

No genuine CW signals can be claimed from these analyses. Therefore, we proceeded to establish 95% confidence-level upper limits in selected frequency bands and orbital parameter ranges, while also evaluating overall sensitivity, with the most stringent value being $h_0 \approx 5.64 \times 10^{-26}$ at $f \approx 229.5 \text{ Hz}$ for the search with Livingston data.

Acknowledgments

This research has made use of data or software obtained from the Gravitational Wave Open Science Center [48], a service of the LIGO Scientific Collaboration, the Virgo Collaboration, and KAGRA. This material is based upon work supported by NSF’s LIGO Laboratory which is a major facility fully funded by the National Science Foundation, as well as the Science and Technology Facilities Council of the United Kingdom, the Max-Planck-Society, and the State of Niedersachsen/Germany for support of the construction of Advanced LIGO and construction and operation of the GEO600 detector. Additional support for Advanced LIGO was provided by the Australian Research Council. Virgo is funded, through the European Gravitational Observatory, by the French Centre National de Recherche Scientifique, the Italian Istituto Nazionale di Fisica Nucleare and the Dutch Nikhef, with contributions by institutions from Belgium, Germany, Greece, Hungary, Ireland, Japan, Monaco, Poland, Portugal, Spain. KAGRA is supported by Ministry of Education, Culture, Sports, Science and Technology, Japan Society for the Promotion of Science in Japan; National Research Foundation and Ministry of Science and ICT in Korea; Academia Sinica and National Science and Technology Council in Taiwan.

We would like to acknowledge CNAF for providing the computational resources.

Appendix A. DS threshold estimation

A critical aspect of the search was determining the correct DS threshold. Assuming the GW data is dominated by Gaussian noise with standard deviation σ , the distribution of the DS, \mathcal{S} , should follow the probability distribution given in (20). However, instrumental lines and data gaps introduce deviations from this expected behaviour, which are more pronounced in the tail of the distribution, particularly when \mathcal{S} is large. As noise artifacts can significantly influence the DS threshold calculation, it is essential to compute it accurately to reliably identify significant candidates.

Using the known instrumental-line frequencies from O3 [43], we calculate the Doppler broadening effect, ΔM , induced by binary demodulation corrections and Earth’s revolution corrections ΔM_{T} ($\sim 10^{-4}$), i.e.: [34]

$$\Delta M_{\text{tot}} = \frac{a_{\text{p}}\Omega}{1 - e} + \Delta M_{\text{T}}. \quad (\text{A.1})$$

This effect shifts the left edge of the broadened region by ΔM_{tot} to the left and the right edge by ΔM_{tot} to the right. For example, in figure A1, we illustrate this for a 508.5 Hz injected Scorpius X-1-like signal with $H_0 = 1 \times 10^{-24}$ in the band [508, 509] Hz. In this case, two instrumental lines have been Doppler broadened due to the demodulation correction, causing them to overlap when computing the DS.

Rather than removing the entire Doppler-modulated intervals for all instrumental lines, we opted to compute the DS threshold using a dataset where the instrumental lines are set to zero.

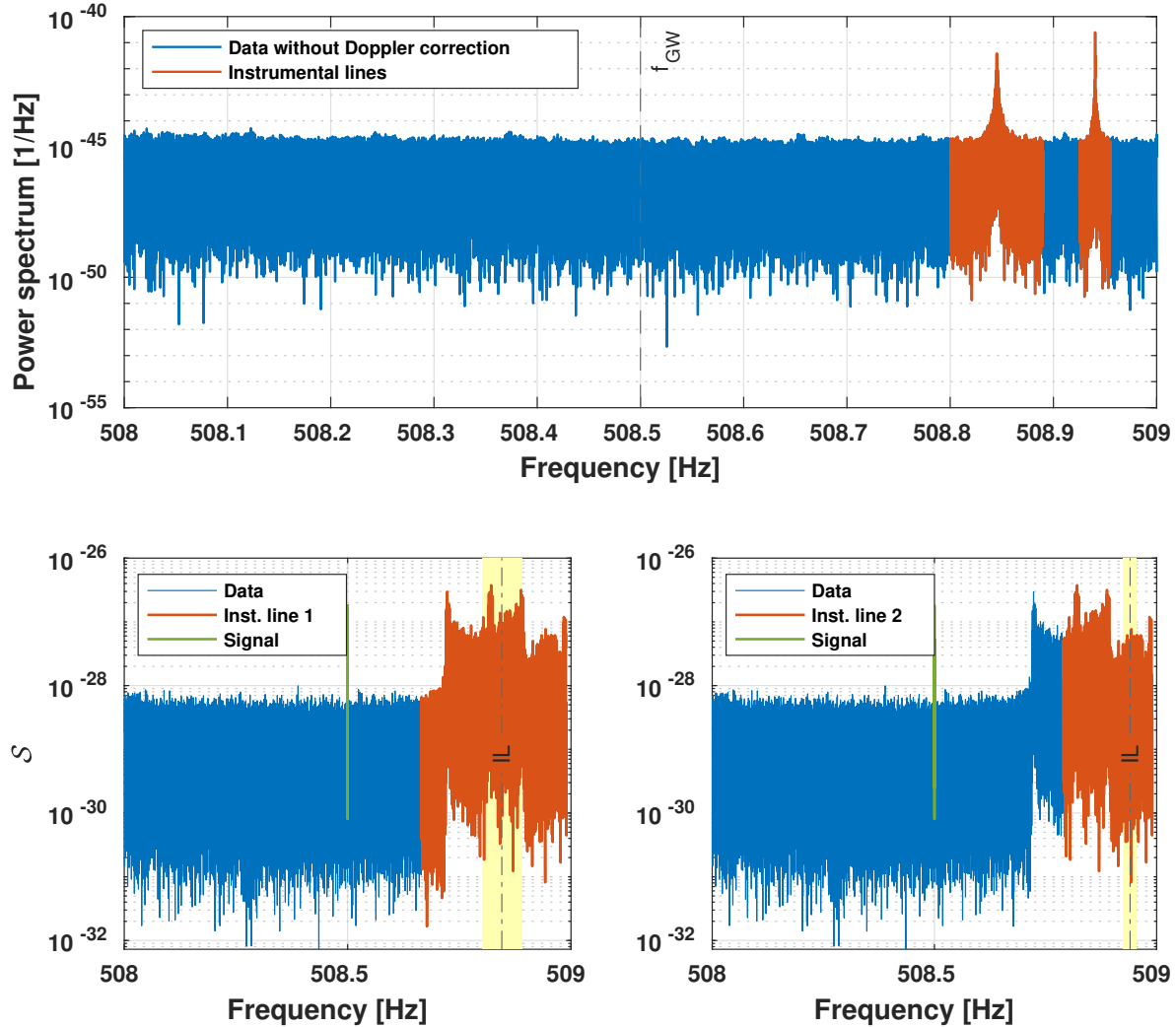


Figure A1. CW signal injected in 10 days of Hanford O3 data, with strain $H_0 = 1 \times 10^{-24}$, $f_{\text{GW}} = 508.5$ Hz, orbital parameters $P = 68023.92$ s, $a_p = 1.8$ ls, $e = 0.0132$, $\omega = 45.1^\circ$ and $t_p = 1078165521$ GPS. Power spectrum of (both Earth and binary Doppler) modulated data. The two orange instrumental lines at ~ 508.85 Hz and ~ 508.95 Hz (catalogued both as “Violin mode 1st harmonic” in [43]) are visible and are marked in orange. *Bottom:* DS after demodulating the data according to the description in section 3. On the *left (right)* we highlight in orange the broadened band of the *first (second)* instrumental line. Because of their overlap, the lines are not plotted together. In both cases, the yellow band indicates the original width of the instrumental line for reference.

Once the instrumental lines are removed, we can compute the normalized histogram of the DS distribution within a given band, which is expected to follow the form given in (19). However, this analytical function does not provide a good fit for the higher values of \mathcal{S} , as the assumption of purely Gaussian noise breaks down at these levels. To account for the non-Gaussian nature of the data, we can approximate the behavior of (19) at large values of \mathcal{S} with

$$f(\mathcal{S}) \sim Ue^{-q\mathcal{S}}, \tag{A.2}$$

with U and q two constants that must be obtained fitting the data distribution. Additionally, the highly discrete nature of the data makes it challenging to accurately fit the tail of the distribution with (A.2) or any other reliable representation of the behavior of $f(\mathcal{S})$. As a result, we excluded the largest DS values from the fit, removing the top 15% of the data. Specifically, the fitting procedure was performed on the data interval corresponding to the 45th to 85th percentiles of the DS distribution. This choice was made to avoid the influence of extreme values that could distort the fitting process, as suggested in previous resampling studies.

As shown in figure A2, the exponential fit provides a better match to the tail of the distribution in the data presented in figure A1. This data was obtained after removing the instrumental lines and without performing any signal injection, highlighting the effectiveness of the fit in capturing the behavior of the tail.

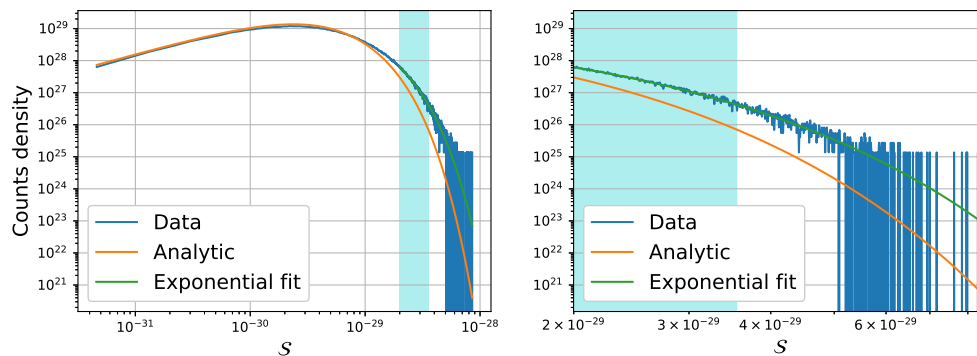


Figure A2. *Left:* The DS frequency histogram computed for the [508, 509] Hz band, based on the same data from figure A1, with instrumental lines removed and no signal injection applied. The analytic function (19) is shown in orange, while the exponential fit using (A.2) is depicted in green. The region selected for the exponential fit is highlighted in turquoise. *Right:* A zoomed-in view of the left plot around $\mathcal{S} \sim 10^{-29}$.

By fitting the function (A.2) to the data in logarithmic scale, we can determine the constants U and q , which are dependent on factors such as the source template, noise characteristics, and potential data artifacts with unknown origins. This allows us to compute the probability of obtaining a DS value larger than a given threshold \mathcal{S}^* , i.e.:

$$P(\mathcal{S} > \mathcal{S}^*) = \int_{\mathcal{S}^*}^{\infty} f(\mathcal{S})d\mathcal{S} = \frac{Ue^{-q\mathcal{S}^*}}{q}. \quad (\text{A.3})$$

However, before using (A.3) at a given FAR to compute \mathcal{S}^* , we need to account for the *look-elsewhere* using (21). Hence, (A.2) can be used to compute the threshold \mathcal{S}^* as

$$\mathcal{S}^* = -\frac{1}{q} \log\left(\frac{q}{U}\text{NFAR}\right). \quad (\text{A.4})$$

The effect of removing the instrumental lines is illustrated in figure A3, using the same dataset as in figure A1.

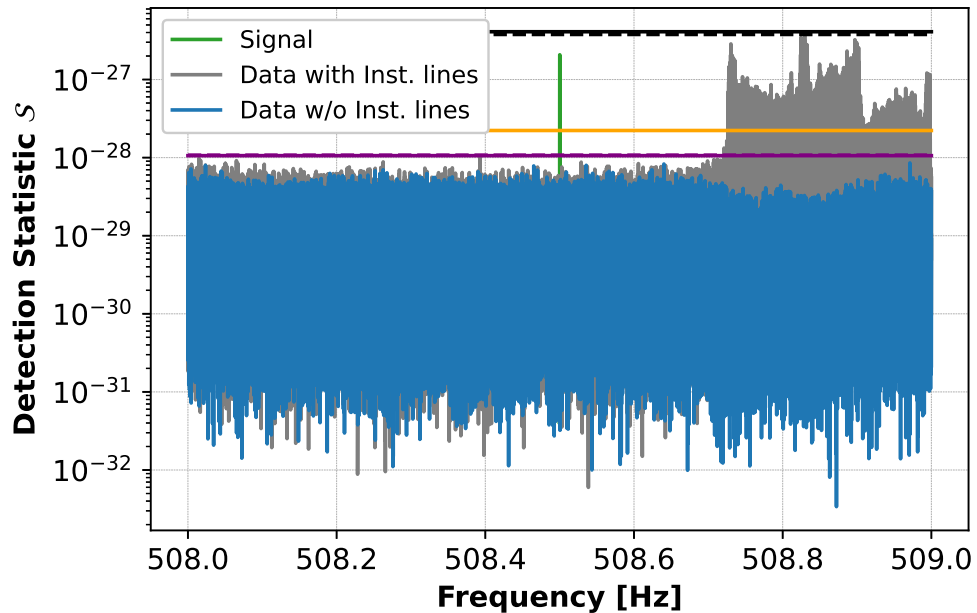


Figure A3. DS values versus frequency for 10 days of Hanford data, comparing results with (gray lines) and without (blue lines) the removal of instrumental lines, based on the resampled dataset from figure A1. The \mathcal{S}^* values are shown as horizontal lines for five different cases: a solid black (purple) line at $\mathcal{S} \approx 4.09 \times 10^{-27}$ ($\mathcal{S} \approx 1.07 \times 10^{-28}$) for an injected Scorpius X-1-like signal with (without) instrumental lines present; a dashed black (purple) line at $\mathcal{S} \approx 3.78 \times 10^{-27}$ ($\mathcal{S} \approx 1.06 \times 10^{-28}$) for an injected Scorpius X-1-like signal with (without) instrumental lines removed; and finally, an orange line at $\mathcal{S} \approx 2.25 \times 10^{-28}$ representing the threshold obtained using simulated Gaussian noise data (this dataset is not shown in the plot).

As shown in figure A3, the removal of instrumental lines has a significant impact on the DS threshold estimation, reducing it by more than an order of magnitude. Specifically, the threshold drops from $\sim 4.09 \times 10^{-27}$ (with instrumental lines) to $\sim 1.06 \times 10^{-28}$ (after removing the lines), while the effect of the simulated signal is negligible, shifting from $\sim 3.78 \times 10^{-27}$ to $\sim 1.07 \times 10^{-28}$ in figure A3. For comparison, we also estimated the DS threshold using only Gaussian noise, with an ASD value of $\sim 8.4 \times 10^{-24} \frac{1}{\sqrt{\text{Hz}}}$ (for the Hanford detector) in the frequency range [508, 509] Hz [47]. This yielded a threshold of $\mathcal{S}^* \approx 2.25 \times 10^{-28}$. Therefore, the removal of instrumental lines leads to a DS threshold that is slightly lower than the value obtained from pure Gaussian noise ($\mathcal{S}^* \sim 2.25 \times 10^{-28}$). Setting a threshold without first removing the instrumental lines would have prevented the recovery of the injected signal.

We applied the procedure described above to the entire frequency band [10, 1000] Hz using the real O3 1-year dataset, while setting all known instrumental lines to zero and demodulating the data with the Scorpius X-1 parameters from table 3. For every 1 Hz band, we observed a wide range of DS threshold values, varying from approximately $\mathcal{O}(10^{-18})$ to $\mathcal{O}(10^{-24})$. Consequently, a rigorous approach would require the use of an adaptive threshold that depends on the specific frequency band being analyzed. Hence, rather than using \mathcal{S} , as defined in [36], we compute \mathcal{S}' defined in (22), as introduced in [14], to better account for the specific characteristics of our analysis. We use \mathcal{S}' in

(22) because the noise-only distribution is normalized in \mathcal{S}' [49], which enhances the robustness of the analysis across multiple detectors and varying frequency bands. The values of \mathcal{S} and \mathcal{S}' as a function of the frequency are shown in figure A4.

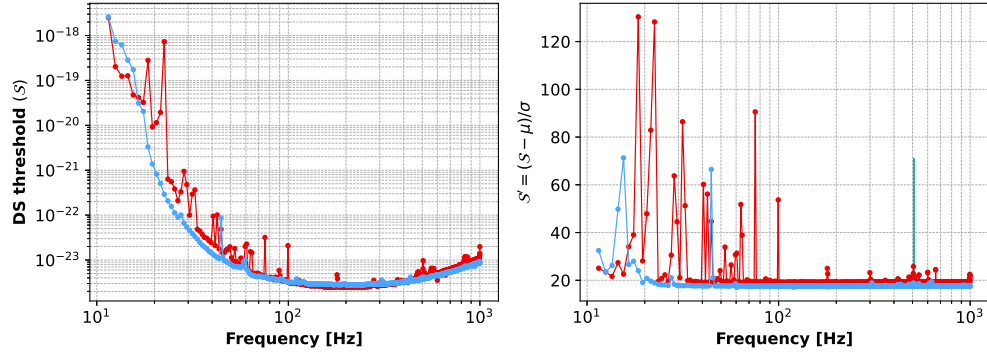


Figure A4. DS threshold \mathcal{S}^* (Left plot) and \mathcal{S}'^* (Right plot) versus frequency, both for Hanford (red line) and Livingston (blue line) detectors. A data point is obtained for every 1 Hz band, which is then plotted. In the Livingston [508, 515] Hz band there are no data to compute the DS threshold as the whole band is contaminated by instrumental lines, which -we remind- have been set to zero only for the DS threshold estimation.

As an example, in the [100, 130] Hz band, which is relatively clean, the mean value of \mathcal{S}'^* for the two detectors is

$$\text{Hanford : } \quad \langle \mathcal{S}'^* \rangle \approx 19.2, \quad (\text{A.5})$$

$$\text{Livingston : } \quad \langle \mathcal{S}'^* \rangle \approx 17.6. \quad (\text{A.6})$$

Therefore, we choose $\mathcal{S}' = 18$ as a reasonable threshold value for the real O3 search. This value is consistent with the results reported in [14] for a previous LIGO-Virgo-KAGRA run. It is important to emphasize that this check is essential, as the DS threshold, \mathcal{S}'^* , must be recalculated each time a new LIGO-Virgo-KAGRA observing run dataset is analyzed.

Appendix B. Testing with Hardware injections

To validate the implementation of the resampling technique, we use hardware injections present in O3 data [48]. These injections refer to simulated GW signals introduced by physically displacing the test masses of detectors, effectively mimicking their response to real GW signals [48]. During the O3 observing run, 17 hardware injections simulating CW signals from rapidly rotating NSs were introduced in the two LIGO detectors. The specific parameters for each injected pulsar are listed in [44]. Out of the 17 injected signals, only pulsars 16 and 17 are associated with binary systems, while the others simulate isolated NS signals. The detailed injection parameters are provided in table B1. Notice that the injected binary pulsars have no spindown terms, although spindown term contributions are, in any case, already well implemented in the resampling pipeline.

Table B1. Parameters of hardware-injected binary pulsars in the LIGO Detectors.

Parameter	Units	Pulsar 16	Pulsar 17
α	rad	-0.2729743	-0.2729743
δ	rad	0.3487022	1.9194985
f_{GW}	Hz	234.567	890.123
h_0		$\sim 1.59 \times 10^{-25}$	$\sim 8.39 \times 10^{-26}$
ψ	rad	4.084	4.084
t_{rot}	rad	0.7598222219515758	0.7675866198953613
a_p	ls	2.35	2.35
t_p	GPS s	1230336018	1230379218
P	s	83941.2	83941.2
e		0.0	0.0
ω	rad	1.23456	2.13456

Using data from the first 31 days of the O3 run, we successfully detected pulsar 16 by identifying one or more candidates that survived to the three coincidence veto, and that are found in five of the nine expected frequency bins (see figure B1). However, despite analyzing the full O3 dataset, we did not detect pulsar 17. While we identified three candidates surviving the DS veto in Livingston and one in Hanford, these candidates did not pass the coincidence veto, preventing a confirmed recovery.

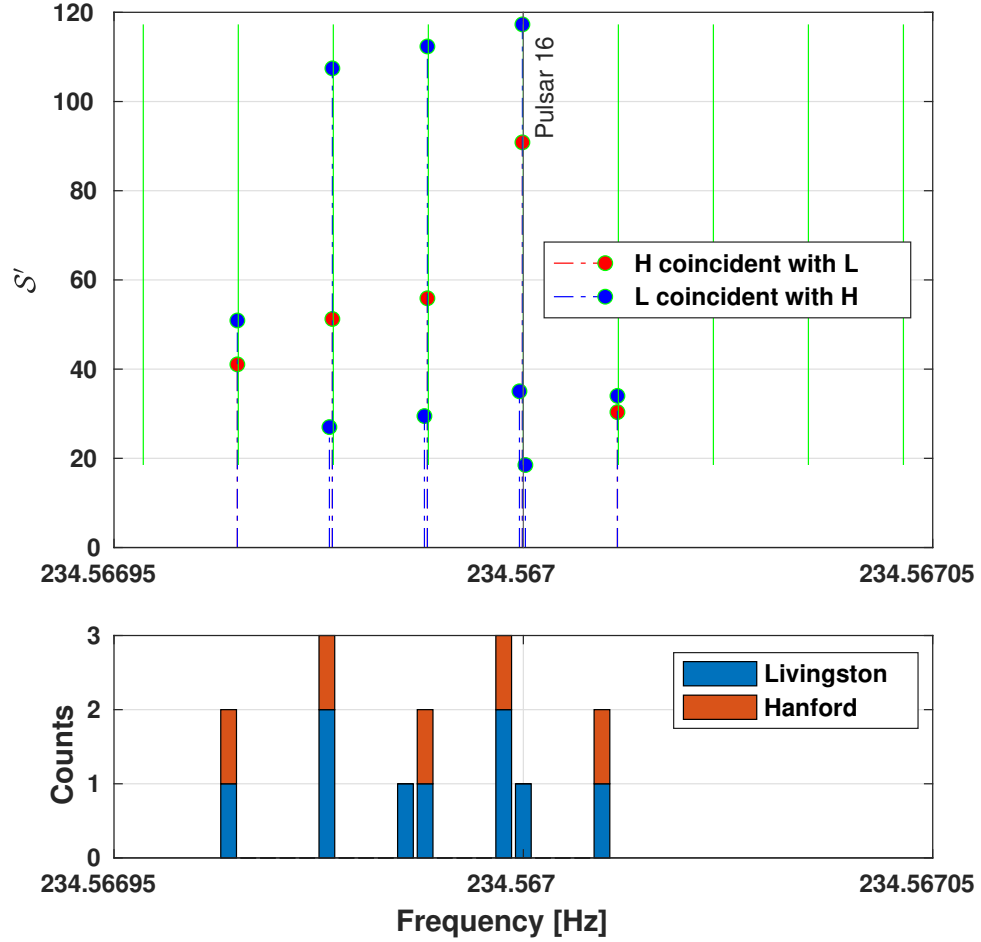


Figure B1. *Top:* The S' values for candidates that survived the coincidence veto with $n_{\text{coin}} = 3$ and $S'^* = 18$ are shown after demodulating the data using the pulsar 16 hardware injection parameters. The green vertical lines mark the expected frequencies of the nine peaks, while the vertical black line at 234.567 Hz indicates the frequency of the hardware injection. *Bottom:* Stacked histogram showing the frequency distribution of the candidates for both Hanford and Livingston detectors.

Appendix C. Computational cost

We detail the computational budget required by the resampling algorithm. The bulk of the computation was performed on the CNAF cluster, using various x86_64 architecture CPUs, including the AMD EPYC 7351 16-Core Processor. Each detector and 1 Hz frequency band required approximately 14.5 GB of memory (RAM + swap) for processing [46]. The total computational time, \mathcal{C}_{tot} , and disk space, \mathcal{D}_{tot} , can be estimated as the sum of computational resources required for each individual step in the analysis: extracting the 1 Hz bands ($\mathcal{Y}_{1\text{Hzband}}$), performing the time-domain resampling ($\mathcal{Y}_{\text{resamp}}$), computing the DS (\mathcal{Y}_{DS}), and applying the coincidence veto ($\mathcal{Y}_{\text{coin}}$). Hence, we can express the total resources as

$$\mathcal{C}_{\text{tot}} = \mathcal{C}_{1\text{Hzband}} + \mathcal{C}_{\text{resamp}} + \mathcal{C}_{\text{DS}} + \mathcal{C}_{\text{coin}} \quad (\text{C.1})$$

$$\mathcal{D}_{\text{tot}} = \mathcal{D}_{1\text{Hzband}} + \mathcal{D}_{\text{resamp}} + \mathcal{D}_{\text{DS}} + \mathcal{D}_{\text{coin}} \quad (\text{C.2})$$

where $\mathcal{Y} \in \{\mathcal{C}, \mathcal{D}\}$. For $T_{\text{obs}} = 1$ year in the O3 run, for 1 Hz band, the computing cost values we obtained are reported in table C1. The values of \mathcal{D} are null in the real search and depend on the number of identified candidates. However, they can be estimated to be approximately 1.2 kB per Hz band if any candidates survive the three-coincidence veto in that band.

Table C1. The CPU time and disk space required for the various steps outlined above were estimated based on a real one-year O3 search conducted for each 1 Hz band in a single detector.

\mathcal{Y}	\mathcal{C}	\mathcal{D}
$\mathcal{Y}_{1\text{Hzband}}$	32.97 m	351 MB
$\mathcal{Y}_{\text{resamp}}$	6.87 h	336 MB
\mathcal{Y}_{DS}	3.11 m	1.5 GB
$\mathcal{Y}_{\text{coinc}}$	20.3 s	//

We note that the worst impact on the time cost comes from the resampling step. As explained in [14], the computational resource needed to extract 1 Hz band can be expressed as

$$\mathcal{C}_{1\text{Hzband}} = c_{1\text{Hzband}} N_f N_{\text{det}} T_{\text{obs}}[\text{d}], \quad (\text{C.3})$$

$$\mathcal{D}_{1\text{Hzband}} = d_{1\text{Hzband}} N_f N_{\text{det}} T_{\text{obs}}[\text{d}], \quad (\text{C.4})$$

with N_f the number of 1 Hz frequency bands, N_{det} the number of detectors and T_{obs} the observation time in days. Hence, using the values of table C1 with $N_f = 1$, $N_{\text{det}} = 1$ and $T_{\text{obs}} = 361$ days, i.e., the number of days between the start and the end of O3, in (C.3) and (C.4), we get $c_{1\text{Hzband}} = 5.48$ s and $d_{1\text{Hzband}} = 970$ kB. For the steps following the 1 Hz band extraction, the computational resources required (both in terms of computing time and disk space) grow with the number of points N_p in the search parameter space. For example, in the research presented in this paper, we covered three set of parameter space, hence $N_p = 3$. Therefore we have:

$$\mathcal{C}_{\text{resamp}} = c_{\text{resamp}} N_f N_{\text{det}} T_{\text{obs}}[\text{d}] N_p, \quad (\text{C.5})$$

$$\mathcal{D}_{\text{resamp}} = d_{\text{resamp}} N_f N_{\text{det}} T_{\text{obs}}[\text{d}] N_p, \quad (\text{C.6})$$

$$\mathcal{C}_{\text{DS}} = c_{\text{DS}} N_f N_{\text{det}} T_{\text{obs}}[\text{d}] N_p, \quad (\text{C.7})$$

$$\mathcal{D}_{\text{DS}} = d_{\text{DS}} N_f N_{\text{det}} T_{\text{obs}}[\text{d}] N_p, \quad (\text{C.8})$$

$$\mathcal{C}_{\text{coinc}} = c_{\text{coinc}} N_f N_{\text{det}} T_{\text{obs}}[\text{d}] N_p \quad (\text{C.9})$$

Using again the values in table C1 with $N_p = 1$ in (C.5)-(C.9), we get $c_{\text{resamp}} = 68.6$ s, $d_{\text{resamp}} = 930$ kB, $c_{\text{DS}} = 0.52$ s, $d_{\text{DS}} = 4.16$ MB and $c_{\text{coinc}} = 8.61$ ms.

For the search presented in this paper, considering one set of parameters and considering both detectors, i.e., $N_f = 990$, $N_p = 1$, $N_{\text{det}} = 2$, $T_{\text{obs}} = 361\text{d}$, we get $\mathcal{C}_{\text{tot}} = 148\,195$ CPU h and $\mathcal{D}_{\text{tot}} = 4.33$ TB.

References

- [1] Einstein A 1916 *Sitzungsberichte der Königlich Preussischen Akademie der Wissenschaften* 688–696
- [2] Einstein A 1918 *Sitzungsberichte der Königlich Preussischen Akademie der Wissenschaften* 154–167
- [3] Abbott B P *et al.* (LIGO Scientific Collaboration and Virgo Collaboration) 2016 *Phys. Rev. Lett.* **116**(6) 061102 URL <https://link.aps.org/doi/10.1103/PhysRevLett.116.061102>
- [4] Collaboration T L S *et al.* 2015 *Classical and Quantum Gravity* **32** 074001 URL <https://dx.doi.org/10.1088/0264-9381/32/7/074001>
- [5] Acernese F *et al.* 2014 *Classical and Quantum Gravity* **32** 024001 URL <https://dx.doi.org/10.1088/0264-9381/32/2/024001>
- [6] Abbott B *et al.* 2019 *Physical Review X* **9** URL <https://doi.org/10.1103/PhysRevX.9.031040>
- [7] Sieniawska M and Bejger M 2019 *Universe* **5** ISSN 2218-1997 URL <https://www.mdpi.com/2218-1997/5/11/217>
- [8] Cutler C 2002 *Phys. Rev. D* **66**(8) 084025 URL <https://link.aps.org/doi/10.1103/PhysRevD.66.084025>
- [9] Zimmermann M and Szedenits E 1979 *Phys. Rev. D* **20**(2) 351–355 URL <https://link.aps.org/doi/10.1103/PhysRevD.20.351>
- [10] Wette K 2023 *Astroparticle Physics* **153** 102880 ISSN 0927-6505 URL <https://www.sciencedirect.com/science/article/pii/S092765052300066X>
- [11] Papaloizou J and Pringle J E 1978 *Monthly Notices of the Royal Astronomical Society* **184** 501–508 ISSN 0035-8711 (*Preprint* <https://academic.oup.com/mnras/article-pdf/184/3/501/18521374/mnras184-0501.pdf>) URL <https://doi.org/10.1093/mnras/184.3.501>
- [12] Bildsten L 1998 *The Astrophysical Journal* **501** L89 URL <https://dx.doi.org/10.1086/311440>
- [13] Wagoner R V 1984 *The Astrophysical Journal* **278** 345–348
- [14] Singhal A *et al.* 2019 *Classical and Quantum Gravity* **36** 205015 URL <https://dx.doi.org/10.1088/1361-6382/ab4367>
- [15] Wang L, Steeghs D, Galloway D K, Marsh T and Casares J 2018 *Monthly Notices of the Royal Astronomical Society* **478** 5174–5183 ISSN 0035-8711 (*Preprint* <https://academic.oup.com/mnras/article-pdf/478/4/5174/25102157/sty1441.pdf>) URL <https://doi.org/10.1093/mnras/sty1441>
- [16] Killestein T L, Mould M, Steeghs D, Casares J, Galloway D K and Whelan J T 2023 *Monthly Notices of the Royal Astronomical Society* **520** 5317–5330 ISSN 0035-8711 (*Preprint* <https://academic.oup.com/mnras/article-pdf/520/4/5317/49329986/stad366.pdf>) URL <https://doi.org/10.1093/mnras/stad366>
- [17] Abbott R *et al.* (LIGO Scientific Collaboration, Virgo Collaboration, and KAGRA Collaboration) 2022 *Phys. Rev. D* **106**(6) 062002 URL <https://link.aps.org/doi/10.1103/PhysRevD.106.062002>
- [18] Vargas A F and Melatos A 2023 Search for gravitational waves from scorpius x-1 with a hidden markov model in o3 ligo data with a corrected orbital ephemeris (*Preprint* [2310.19183](https://arxiv.org/abs/2310.19183)) URL <https://arxiv.org/abs/2310.19183>
- [19] Abbott R *et al.* 2022 *The Astrophysical Journal Letters* **941** L30 URL <https://dx.doi.org/10.3847/2041-8213/aca1b0>
- [20] Whelan J T, Tenorio R, Wofford J K, Clark J A, Daw E J, Goetz E, Keitel D, Neunzert A, Sintes A M, Wagner K J, Woan G, Killestein T L and Steeghs D 2023 *The Astrophysical Journal* **949** 117 URL <https://dx.doi.org/10.3847/1538-4357/acc8d7>
- [21] Wagner K J *et al.* 2022 *Classical and Quantum Gravity* **39** 075013 URL <https://dx.doi.org/10.1088/1361-6382/ac5012>
- [22] Meadors G D *et al.* 2018 *Phys. Rev. D* **97**(4) 044017 URL <https://link.aps.org/doi/10.1103/PhysRevD.97.044017>

- [23] Zhang Y *et al.* 2021 *The Astrophysical Journal Letters* **906** L14 URL <https://dx.doi.org/10.3847/2041-8213/abd256>
- [24] Mukherjee A, Prix R and Wette K 2023 *Phys. Rev. D* **107**(6) 062005 URL <https://link.aps.org/doi/10.1103/PhysRevD.107.062005>
- [25] The LIGO Scientific Collaboration t V C and the KAGRA Collaboration) 2023 *The Astrophysical Journal Supplement Series* **267** 29 URL <https://dx.doi.org/10.3847/1538-4365/acdc9f>
- [26] Gravitational wave open science center: O1, o2 and o3 data sets. <https://gwosc.org/data/> the O3 data run is divided into two runs. O3a Time Range: April 1, 2019 through October 1, 2019. O3b Time Range: November 1, 2019 through March 27, 2020.
- [27] Astone P *et al.* 2010 *Classical and Quantum Gravity* **27** 194016 URL <https://dx.doi.org/10.1088/0264-9381/27/19/194016>
- [28] D'Antonio S, Frasca S and Palomba C 2009 *Classical and Quantum Gravity* **26** 204012 URL <https://dx.doi.org/10.1088/0264-9381/26/20/204012>
- [29] Jaranowski P, Królak A and Schutz B F 1998 *Phys. Rev. D* **58**(6) 063001 URL <https://link.aps.org/doi/10.1103/PhysRevD.58.063001>
- [30] Abbott R *et al.* 2022 *The Astrophysical Journal* **935** 1 URL <https://dx.doi.org/10.3847/1538-4357/ac6acf>
- [31] D'Onofrio L, Astone P, Dal Pra S, D'Antonio S, Di Giovanni M, De Rosa R, Leaci P, Mastrogiovanni S, Mirasola L, Muciaccia F, Palomba C and Pierini L 2024 *Classical and Quantum Gravity* **42** 015005 URL <https://dx.doi.org/10.1088/1361-6382/ad94c5>
- [32] Gaia Collaboration 2020 VizieR Online Data Catalog: Gaia EDR3 (Gaia Collaboration, 2020) VizieR On-line Data Catalog: I/350. Originally published in: 2021A&A...649A...1G; doi:10.5270/esa-lug
- [33] Duflet M, Figon P and Meyssonier N 1995 *Astronomy and Astrophysics Supplement Series* **114** 269
- [34] Leaci P and Prix R 2015 *Phys. Rev. D* **91**(10) 102003 URL <https://link.aps.org/doi/10.1103/PhysRevD.91.102003>
- [35] Leaci P, Astone P, D'Antonio S, Frasca S, Palomba C, Piccinni O and Mastrogiovanni S 2017 *Physical Review D* **95** ISSN 2470-0029 URL <http://dx.doi.org/10.1103/PhysRevD.95.122001>
- [36] Astone P *et al.* 2014 *Phys. Rev. D* **89**(6) 062008 URL <https://link.aps.org/doi/10.1103/PhysRevD.89.062008>
- [37] Taylor J H and Weisberg J M 1989 *The Astrophysical Journal* **345** 434
- [38] Frasca S and Palomba C 2004 *Classical and Quantum Gravity* **21** S1645 URL <https://dx.doi.org/10.1088/0264-9381/21/20/007>
- [39] Mastrogiovanni S, Astone P, D'Antonio S, Frasca S, Intini G, Leaci P, Miller A, Palomba C, Piccinni O J and Singhal A 2017 *Classical and Quantum Gravity* **34** 135007 URL <https://dx.doi.org/10.1088/1361-6382/aa744f>
- [40] Astone P *et al.* 2005 *Classical and Quantum Gravity* **22** S1197 URL <https://dx.doi.org/10.1088/0264-9381/22/18/S34>
- [41] Riles K 2023 *Living Reviews in Relativity* **26** 3 ISSN 1433-8351 URL <https://doi.org/10.1007/s41114-023-00044-3>
- [42] Gross E and Vitells O 2010 *The European Physical Journal C* **70** 525–530 ISSN 1434-6052 URL <https://doi.org/10.1140/epjc/s10052-010-1470-8>
- [43] O3 instrumental lines <https://gwosc.org/O3/o3speclines/>
- [44] O3 continuous wave hardware injections. https://www.gw-openscience.org/O3/o3_inj/
- [45] La Rosa I *et al.* 2021 *Universe* **7** ISSN 2218-1997 URL <https://www.mdpi.com/2218-1997/7/7/218>
- [46] INFN Cluster hpc <https://wiki.infn.it/strutture/cnaf/clusterhpc/home>
- [47] Abbott R *et al.* (LIGO Scientific Collaboration and Virgo Collaboration) 2021 *Phys. Rev. X* **11**(2) 021053 URL <https://link.aps.org/doi/10.1103/PhysRevX.11.021053>
- [48] Biwer C *et al.* 2017 *Phys. Rev. D* **95**(6) 062002 URL

<https://link.aps.org/doi/10.1103/PhysRevD.95.062002>

[49] Astone P o 2014 *Phys. Rev. D* **90**(4) 042002 URL <https://link.aps.org/doi/10.1103/PhysRevD.90.042002>